https://doi.org/10.5194/egusphere-2023-509
Preprint. Discussion started: 4 April 2023

Regional mapping of energetic short mesoscale ocean dynamics from altimetry: performances from real observations.

Florian Le Guillou[1], Lucile Gaultier[2], Maxime Ballarotta[3], Sammy Metref[4], Clément Ubelmann[4], Emmanuel Cosme[5], and Marie-Helène Rio[1]

[1]European Space Agency (ESA), Frascati, Italy
[2]OceanDataLab, Brest, France
[3]Collecte Localisation Satellite, Ramonville Saint-Agne, France
[4]Datlas, Grenoble, France
[5]Univ. Grenoble Alpes, CNRS, IRD, Grenoble INP, IGE, Grenoble, F-38000, France

Correspondence: Florian Le Guillou (florian.leguillou@esa.int)

Abstract. For over 25 years, satellite altimetry has provided invaluable information about the ocean dynamics at many scales. In particular, gridded Sea Surface Height (SSH) maps allow to estimate the mesoscale geostrophic circulation in the ocean. However, conventional interpolation techniques rely on static optimal interpolation schemes, hence limiting the estimation of non linear dynamics at scales not well sampled by altimetry (i.e. below 150-200km at mid latitudes). To overcome this limitation in the resolution of small-scale SSH structures (and thus small-scale geostrophic currents), a Back and Forth Nudging algorithm combined with a Quasi-Geostrophic model, a technique called BFN-QG, has been successfully applied on simulated SSH data in Observing System Simulation Experiments (OSSEs), showing a significant reduction in interpolation error and an improvement of space-time resolutions of the experimental gridded product compared to operational products. In this study, we propose to apply the BFN-QG to real altimetric SSH data in a highly turbulent region spanning a part of the Agulhas current. The performances are evaluated within Observing System Experiments (OSEs) that use independent data (such as independent SSH, Sea Surface Temperature and drifter data) as ground-truth. By comparing the mapping performances to the ones obtained by operational products, we show that the BFN-QG improves the mapping of short, energetic mesoscale structures and associated geostrophic currents both in space and time. In particular, the BFN-QG improves (i) the spatial effective resolution of the SSH maps by a factor of 20%, (ii) the zonal and (especially) the meridional geostrophic currents and (iii) the prediction of Lagrangian transport for lead times up to 10 days. Unlike the results obtained in the OSSEs, the OSEs reveal more contrasting performances in low variability regions that are discussed in the paper.

1 Introduction

Ocean circulation drives most of the global heat and mass transport, greatly impacting climate, biodiversity and human activities. In the open ocean, most of the kinetic energy is contained in mesoscale (50-500 km) structures (Ferrari and Wunsch, 2009). In particular, mesoscale eddies can transport heat and nutrients through very long distances and time (Fu et al., 2010).

https://doi.org/10.5194/egusphere-2023-509
Preprint. Discussion started: 4 April 2023

Satellite altimetry is the only observing system capable of documenting mesoscale ocean geostrophic currents with consistent temporal and spatial resolution. By merging several altimetric datasets into gridded Sea Surface Height (SSH) maps, geostrophic velocities can be derived (Ducet et al., 2000). Today, one of the commonly used gridded SSH maps are the DUACS products, distributed by the Copernicus Marine Environment Monitoring Service (CMEMS). The mapping algorithm is based on a space-time optimal interpolation (OI) of the available altimetric SSH satellite data (Le Traon et al., 1998). These maps resolve oceanic processes down to 150-200km in wavelength at mid-latitudes (Ballarotta et al., 2019).

The maps designed by the DUACS system provide little information about short mesoscale dynamics (<200 km). In fact, these fine scales are mostly governed by nonlinear dynamics, which makes the (linear) OI hardly effective given the relative sparseness of observations. Yet, it is known from other observations and numerical models that these fine scales play a major role in ocean circulation (Su et al., 2018). Recent efforts have been made to improve the space-time resolutions of the SSH maps. Ubelmann et al. (2015) proposed to add a dynamical constraint based on the conservation of the potential vorticity in the OI procedure. This improved algorithm, called Dynamical Optimal Interpolation (DOI), has been tested with simulated (Ubelmann et al., 2016) and real conventional altimetric data (Ballarotta et al., 2020). The results show a better estimation of fine scale structures that are filtered out in the conventional DUACS system.

Motivated by the very recent Surface Water and Ocean Topography (SWOT) mission, Le Guillou et al. (2021a) have proposed a data assimilation algorithm (called the Back and Forth Nudging) operating with a 1.5-layer quasi geostrophic model (the same as the one used in the DOI) to benefit from the high spatial resolution of SWOT, while compensating for its low temporal resolution, in the design of SSH maps. The technique, referred to as BFN-QG, has been tested in an Observatory Simulation System Experiment (OSSE) with simulated SWOT and conventional altimeter data. The authors have shown a net improvement of the resolutions of maps both with conventional altimeter and SWOT data, in comparison with the DUACS algorithm. In addition to these good performances w.r.t. DUACS, the BFN-QG works at a relatively low computational cost thanks to the simplicity of the algorithm.

In this paper, we continue the work of Le Guillou et al. (2021a) by exploring the performances of the BFN-QG algorithm for mapping real conventional altimetry data. Both the BFN-QG and DUACS systems are applied in a study area that spans a part of the energetic Agulhas current. The performances are assessed with independent SSH satellite data, *in situ* velocity from drifters and Sea-Surface-Temperature (SST) data. We will show that the SSH maps computed from the BFN-QG reveal short energetic mesoscale ocean dynamic structures in better agreement with the independent data compared to DUACS. The paper is organized as follows: first we recall the main features of the BFN-QG and its implementation with real SSH data; second we present the experimental setup designed to assess the mapping performances; third we report the performances both in mapping SSH and geostrophic current and finally we discuss the results by giving some perspectives for future works.

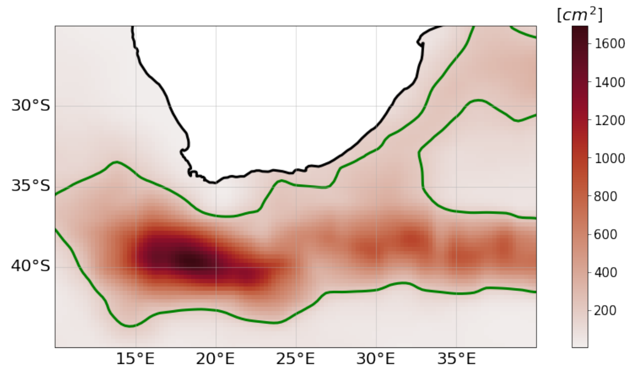

Figure 1. 10-year mean variance of SSH computed from DUACS L4 product on the study region. To later help the result interpretation, the green contour corresponds to the 200 cm^2 SSH variance, depicting the limit between high and low energetic areas.

2 The BFN-QG algorithm

2.1 The QG dynamics

The dynamics of SSH is simulated by a 1.5-layer Quasi-Geostrophic (QG) model. This model simulates the dynamics of the first baroclinic mode, known to capture most of the SSH variability. In this model, the conserved potential vorticity q is diagnosed from SSH :

$$q = \nabla^2 \psi - \frac{1}{L_D^2}\psi \tag{1}$$

with L_D the Rossby radius of deformation, $\nabla^2 = \frac{\partial^2}{\partial x^2} + \frac{\partial^2}{\partial y^2}$, and ψ the streamfunction such as:

$$\psi = \frac{g}{f} SSH \tag{2}$$

g being the gravity constant and f the Coriolis frequency.

The conservation of potential vorticity is written:

$$\frac{\partial q}{\partial t} + \mathbf{u_g} \cdot \nabla q = 0 \tag{3}$$

where $\mathbf{u_g}$ is the geostrophic velocity vector diagnosed from SSH:

$$\mathbf{u_g} = -\mathbf{k} \times \psi = -\frac{g}{f_0} \mathbf{k} \times \nabla SSH \tag{4}$$

where $\mathbf{k}$ denotes the vertical direction and $\nabla = (\frac{\partial}{\partial x}, \frac{\partial}{\partial y})$.

2.2 Formulation with Sea Level Anomalies

In reality, an altimeter only provides accurate observations of the time-fluctuating part of SSH, called Sea Level Anomaly (SLA). The time-averaged SSH, called Mean Dynamical Topography (MDT) is computed with the combination of *in situ* data

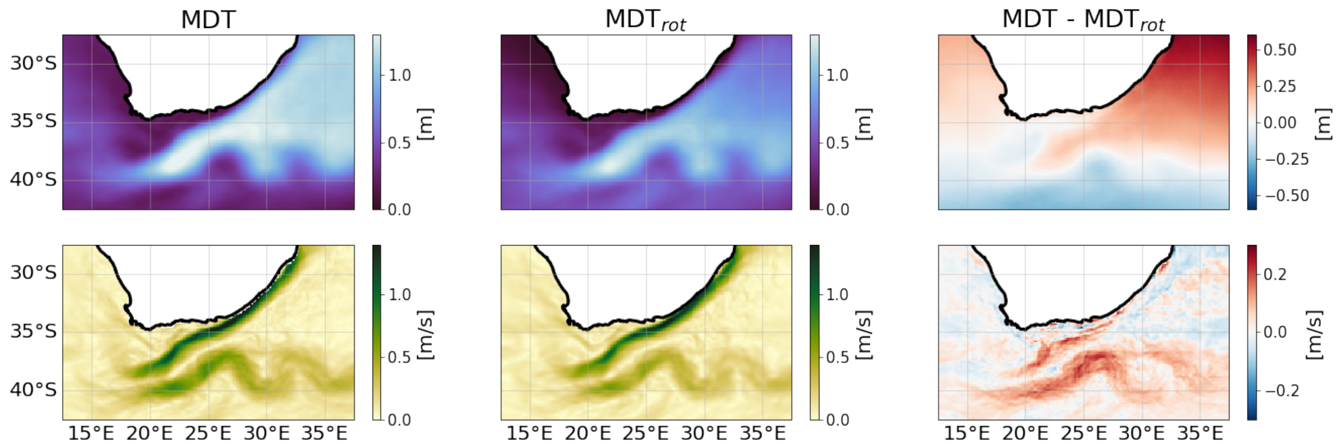

Figure 2. Top: raw MDT field (left), its rotational part (middle) and the difference between the two (right). Bottom: absolute geostrophic velocity computed from the associated top fields using Eq.4.

and other satellite observations (Mulet et al., 2021). Then:

$$SSH = MDT + SLA \tag{5}$$

70 To formulate the QG dynamics with SLA, we decompose the geostrophic flow and the potential vorticity using the Reynolds decomposition:

$$\mathbf{u_g} = \overline{\mathbf{u_g}} + \mathbf{u_g}' \tag{6a}$$

$$q = \overline{q} + q' \tag{6b}$$

where $\overline{\mathbf{u_g}}$ and $\overline{q}$ stand for the mean components (SLA-independent) and $\mathbf{u}'_\mathbf{g}$ and q' the time-fluctuating components (diagnosed

75 from SLA):

$$\mathbf{u_g}' = -\frac{g}{f_0}\mathbf{k} \times \nabla SLA \tag{7a}$$

$$q' = \frac{g}{f_0}\nabla^2 SLA - \frac{g}{f_0 L_D^2} SLA \tag{7b}$$

The prognostic equation for the potential vorticity fluctuation is then:

$$\frac{\partial q'}{\partial t} + \overline{\mathbf{u_g}} \cdot \nabla q' + \mathbf{u}'_\mathbf{g} \cdot \nabla \overline{q} + \mathbf{u}'_\mathbf{g} \cdot \nabla q' = 0 \tag{8}$$

80 **2.3 Data assimilation**

The SLA observations (denoted as SLA^{obs}) are assimilated in the QG model with the Back and Forth Nudging (BFN, Auroux and Blum, 2008) technique. This technique is based on the nudging strategy, which consists in "gently" pulling the model

https://doi.org/10.5194/egusphere-2023-509
Preprint. Discussion started: 4 April 2023

trajectory towards the observations. Mathematically, an extra term proportional to the difference between the model SLA and the observations is added in equation 8:

$$\frac{\partial q'}{\partial t} + \overline{\mathbf{u_g}} \cdot \nabla q' + \mathbf{u}'_{\mathbf{g}} \cdot \nabla \overline{q} + \mathbf{u}'_{\mathbf{g}} \cdot \nabla q' = K(SLA^{obs} - SLA) \tag{9}$$

where K is the tunable nudging coefficient. Its value determines the balance between the weights given to the observations and the QG dynamics. As explained in Le Guillou et al. (2021a), K is varying in time and space to allow a smooth nudging of the model towards the observations. Mathematically, the nudging coefficient at time t and at the model grid point x is computed by the following equation:

$$K(x,t) = K_0 \sum_{i=1}^{N_{obs}} e^{-\left(\frac{||x-x_i||}{D}\right)^2} e^{-\left(\frac{t-t_i}{\tau}\right)^2} \tag{10}$$

where K_0 is the nominal value of the nudging coefficient, N_{obs} is the number of observations, (x_i, t_i) are the space-time coordinates of the i$^{\text{th}}$ observation. D and τ are the space and time scales at which the model is nudged towards the observations, impacting directly the scales of the reconstructed structures.

The BFN algorithm calls iteratively the forward nudging, defined as a forward-in-time propagation of equation 9 with K>0, and the backward nudging, defined as a backward-in-time propagation of equation 9 with K<0, within a fixed temporal window T. The temporal window T has to be chosen considering the observation sampling, the decorrelation time of the QG model, and the computational complexity. At the beginning of each temporal loop, the SLA variable is initialized with the value estimated from the previous loop. In a few iterations (less than 20), the BFN converges towards a trajectory that both fits the observations and the model dynamics. For more details on the BFN-QG technique, the reader can refer to Auroux and Blum (2008), Amraoui et al. (2023) and Le Guillou et al. (2021a).

3 Experimental set-up

3.1 Study area and input data

We assess the BFN-QG performances in a part of the Agulhas current (10–40°E, 25–45°S) from January 1, 2010 to December 31, 2019. Figure 1 shows the mean variance of SSH in the study region computed from the DUACS L4 products and averaged over the ten years time period. The Agulhas current is the major western boundary current of the Southern Hemisphere, transporting large volumes of water from the Indian to the Atlantic ocean, greatly impacting climate (Bryden et al., 2005) and vessel trajectories (Le Goff et al., 2021).

As input data of the BFN-QG, we use the along-track L3 filtered SLA products from Jason-3, Sentinel-3A, Sentinel-3B, HaiYang-2, CryoSat-2 and SARAL/AltiKa. These SLAs have been distributed by the CMEMS (http://marine.copernicus.eu/) after the reprocessing of 25 years of altimetric data (Taburet et al., 2019). For our analysis, we use the spatially filtered data, whose cutoff has been set to 65km, corresponding to altimeters' effective resolution (Pujol et al., 2016).

https://doi.org/10.5194/egusphere-2023-509
Preprint. Discussion started: 4 April 2023

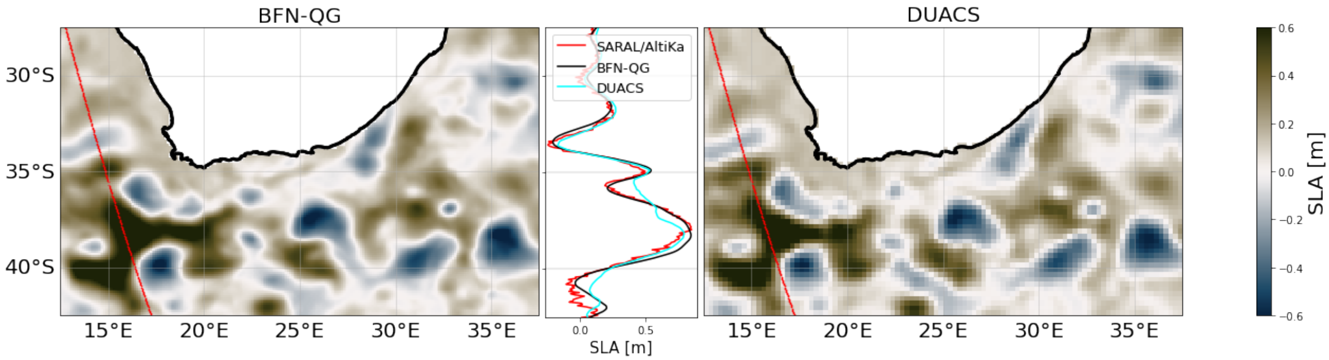

Figure 3. SLA mapped by the BFN-QG (left) and DUACS (right) systems on the 15 October 2019. The fields are plotted with native spatial resolution (0.25° for the DUACS product, 0.1° for the BFN-QG product). The red lines represent the track of the independent SARAL/AltiKa altimeter at this date. The middle panel of the figure compares the 1D SLA profile of the independent with the estimated SLAs interpolated on the track location.

3.2 Mean geostrophic current

The mean state of the ocean surface needed to advect the QG potential vorticity anomaly q' through equation 8 is extracted from the CNES-CLS18 mean dynamic products (Mulet et al., 2021). In this product, the topography (MDT) and velocity (MDV; for Mean Dynamical Velocity) are estimated with a multivariate objective analysis of a combination of altimeter and space gravity data and *in situ* measurements. A central step of the analysis lies in the filtering of the ageostrophic component of the *in situ* velocity measurements.

In equations 8 and 9, both $\overline{\mathbf{u_g}}$ and $\overline{q}$ have to be prescribed. For reasons not investigated during this work, the MDV product is not divergence-free (figure 2). Because $\overline{\mathbf{u_g}}$ must be rotational by construction (gradient of a potential), we prescribe its value with the rotational part of MDV, called MDV$_{rot}$ (bottom middle panel on figure 2). Then, for consistency, $\overline{q}$ is diagnosed through equation 1 by the corresponding MDT$_{rot}$ (top middle panel on figure 2), estimated from MDV$_{rot}$ with a gradient conjugate method. At the end of the mapping processing, we add the full MDV to the estimated velocity anomalies.

3.3 Performances assessment strategies

We compare the performances of the BFN-QG system and the DUACS DT2018 system (Taburet et al., 2019). We use the global daily product provided by CMEMS on a 0.25° longitude x 0.25° latitude grid. The BFN-QG is run on a 0.1° longitude x 0.1° latitude grid and the output maps are saved every 3hrs. The parameters of the BFN-QG (defined in the previous sections) have been prescribed after a sensitivity experiment and are listed in table 1

The comparison focuses on SLA (hereafter called SLA-mapping; see section 4) and geostrophic currents (hereafter called V-mapping; see section 5). For assessing the SLA-mapping capability, we exclude SARAL/AltiKa of the altimetric observation network to use it as independent data and we focus only on the year 2019. For assessing the V-mapping capability, all the

https://doi.org/10.5194/egusphere-2023-509
Preprint. Discussion started: 4 April 2023

Parameter	Description	Value
dx	QG model grid resolution	0.1°
dt	QG model timestep	1200 s
L_D	First Rossby radius of deformation	30 km
$K_0 dt$	(non-dimensionalized) Nudging coefficient	0.7
τ	Nudging space scale	10 km
τ	Nudging time scale	1 days
T	BFN sliding time window length	7 days

Table 1. BFN-QG parameters

available altimetric observation network is used and the validation is performed with independent drifter and SST data over the entire time period (ten years).

4 SLA-mapping performances

The SLA-mapping performances are assessed by comparing the mapped products with the independent altimetric data, following the same method as in Ballarotta et al. (2020). The estimated gridded maps noted $\widehat{SLA}$ are interpolated on the locations of the independent measurements SLA^{ind}. Figure 3 shows an example of two maps estimated by the BFN-QG and DUACS systems and a track of the independent satellite. As the independent data are sparse, the differences $\Delta SLA = \widehat{SLA} - SLA^{ind}$ are aggregated in 1° longitude x 1° latitude boxes to give a spatial distribution of the errors. For each box, we compute the root mean square errors (RMSEs):

$$RMSE = \frac{1}{N}\sum_{i=1}^{N} \Delta SLA[i]^2 \tag{11}$$

where N is the number of independent observations in a specific grid box (left panel of figure 4). Before computing the RMSE, we can apply a spatial filtering on ΔSLA to isolate frequency bands of interest. In our case, we filtered out scales larger than 300km in order to focus on the estimation of mesoscale structures (right panel of figure 4). The comparison of the performances of the BFN-QG versus DUACS is then given by the gain/loss ratio R:

$$R = \frac{RMSE_{\text{BFN-QG}} - RMSE_{\text{DUACS}}}{RMSE_{\text{DUACS}}} \tag{12}$$

The spatial distribution of $RMSE_{\text{BFN-QG}}$ and R for all scales and mesoscales are reported on figure 4.

To evaluate the scale-wise mapping performances, a spectral analysis is carried out and reported on Fig. 5. The analysis is applied on the reconstructed SLAs interpolated on the independent tracks. Each independent satellite track in the study area is split in 800-km segments overlapping every 200km. The data along the segments are then detrended and a Hanning window is applied. We use the Welch (Welch, 1967) method to compute the power spectral density (PSD) distribution for each segments.

https://doi.org/10.5194/egusphere-2023-509
Preprint. Discussion started: 4 April 2023

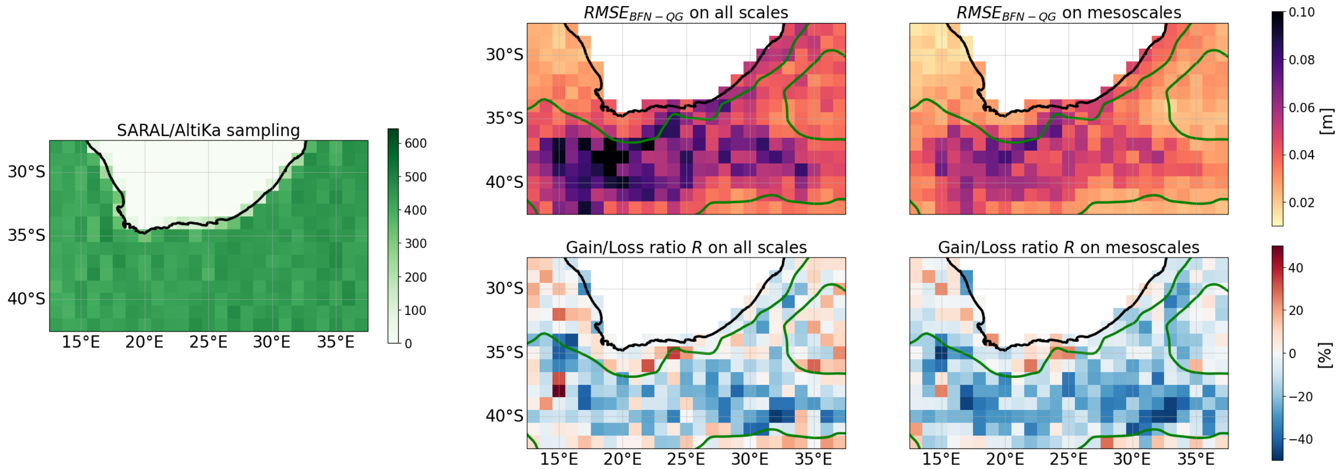

Figure 4. Geographical statistics of the SLA-mapping performances for the year 2019. On the left panel: independent SARAL/AltiKa altimeter sampling. On the right panels: RMSE of the BFN-QG (top) and the gain/loss ratio R with respect to DUACS (bottom) for all spatial scales (left) and mesoscales (right). Negative values (blue) indicate better performances for the BFN-QG method compared to DUACS. The green contour is the 200 cm^2 SSH variance contour.

We average the PSDs for all segments to get a statistically robust estimation of the energy distribution among spatial scales. We compute also the wavelength-dependent PSD score, $SPSD$, defined as:

$$SPSD = 1 - \frac{PSD(\Delta SLA)}{PSD(SLA^{ind})} \tag{13}$$

$SPSD$ is equal to one for a perfect reconstruction and zero when the error is as energetic as the observed oceanic signal. The effective resolution of the maps is defined as the spatial scale for which the spectral score is equal to 0.5. Figure 5 shows the PSDs of the mapped product and the independent data, as well as the associated scores.

The BFN-QG considerably improves the mapping of energetic mesoscale structures compared to DUACS. As shown on figure 4, the improvement (i.e. density and intensity of blue pixels) is higher for mesoscale (defined as scales below 300km) than for all scales. This is corroborated by the spectral analysis which shows that the BFN-QG maps are in better agreement (both in amplitude and phase) with the independent data especially for scales below 300km (figure 5). The effective resolution of the maps is improved by a factor of 20% compared to DUACS. The performances of the BFN-QG are reduced for larger spatial scales and in low variability regions. For scales higher than 300km, DUACS outperforms the BFN-QG on average by a factor of 1.3% (not shown). For all scales, the improvement brought by the BFN-QG is reduced in low variability regions (delimited by the green lines in figure 4). These weak performances of the BFN-QG in reconstructing the large scale structures may be due to the way we compute the nudging coefficient K (through equation 10), whose space and time scales (see table 1) have been tuned to enhance the mapping of short scale dynamics.

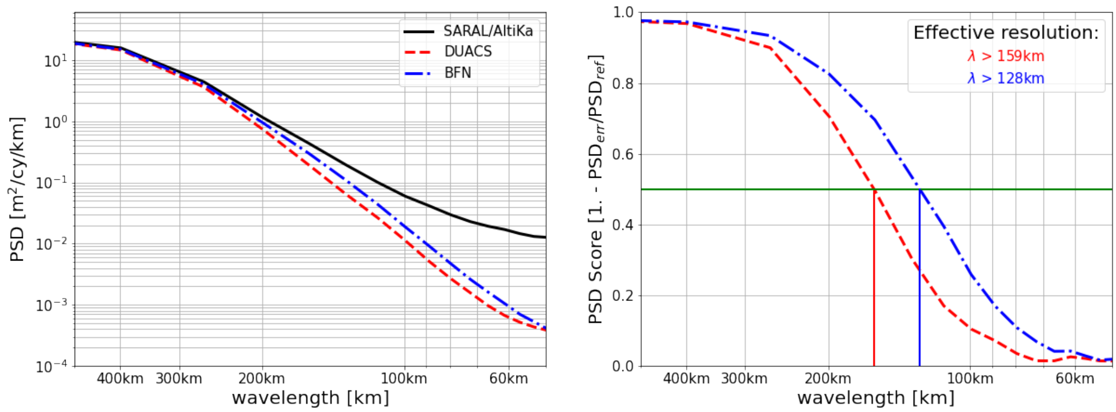

Figure 5. Spectral diagnostics: PSD (left) and associated scores (right) of the mapped products. The intersections between the horizontal green line (corresponding to a PSD score of 0.5) and the curves define the effective resolutions of the products.

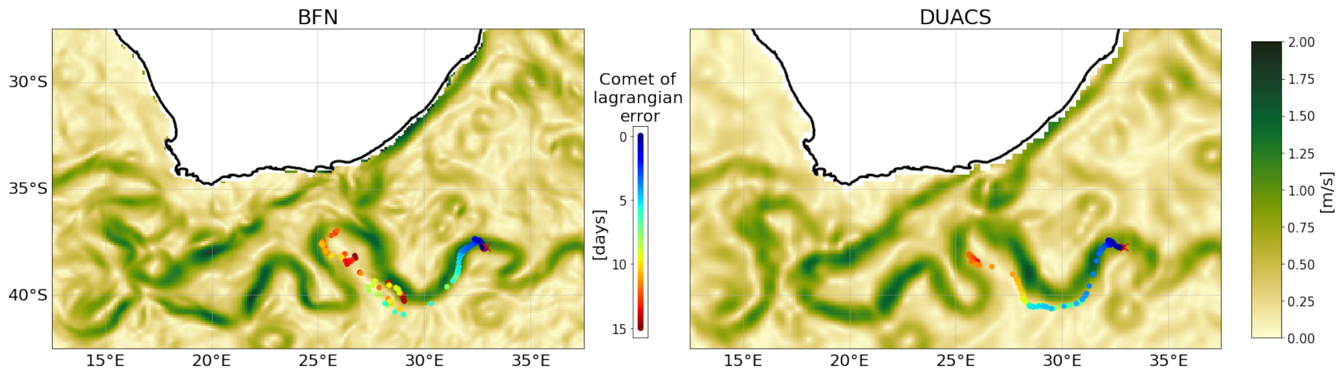

Figure 6. Geostrophic currents mapped by the BFN-QG (left) and DUACS (right) systems on the 2 November 2019. The red cross represents the location of one drifter at this date. The colored dots represent the expected drifter positions as predicted from the true past positions with the mapped currents. Dots' color indicates the prediction lead time. For example, the yellow dots are predictions initialized 9 days in the past. Their distances to the red cross indicate the prediction errors.

5 V-mapping performances

5.1 Validation with drifter data

In this section, the V-mapping performances are assessed by comparing the estimated geostrophic velocities with independent drifter data at hourly resolution (Elipot et al., 2016). The ageostrophic component of the observed velocities has not been removed in these reference data as we assume that it should affect the performance of the DUACS and BFN-QG methods in the same way. Figure 6 illustrates two snapshots of the norm of estimated geostrophic velocities from the BFN-QG and DUACS

https://doi.org/10.5194/egusphere-2023-509
Preprint. Discussion started: 4 April 2023

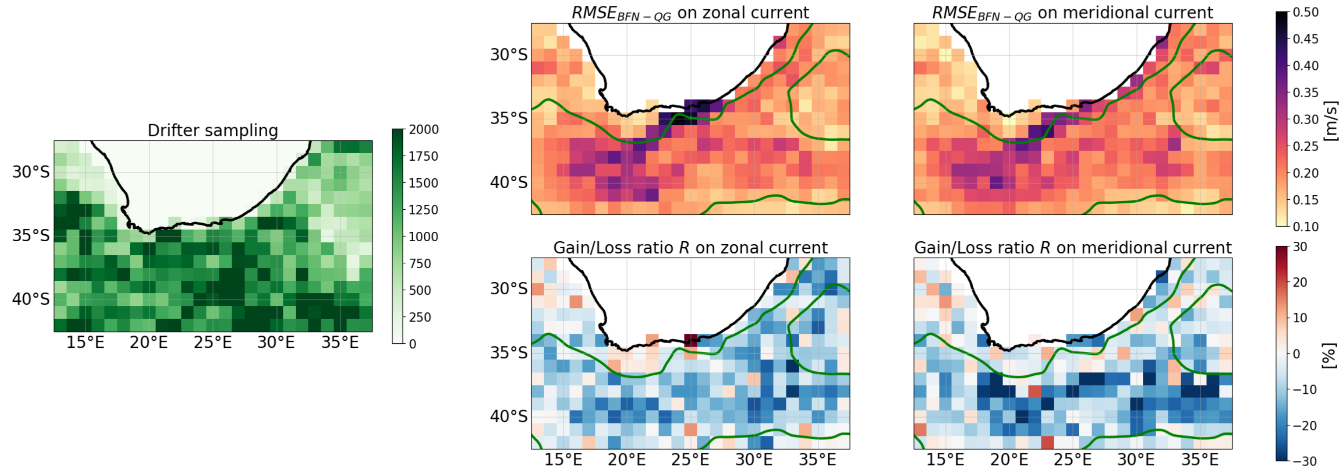

Figure 7. Geographical statistics of the V-mapping performances for the ten years (from 2010 to 2019). On the left panel: independent drifter sampling. On the right panels: RMSE of the BFN-QG (top) and the gain/loss ratio R with respect to DUACS (bottom) for the zonal (left) and meridional (right) currents. Negative values (blue) indicate better performances for the BFN-QG method compared to DUACS. The green contour is the 200 cm^2 SSH variance contour.

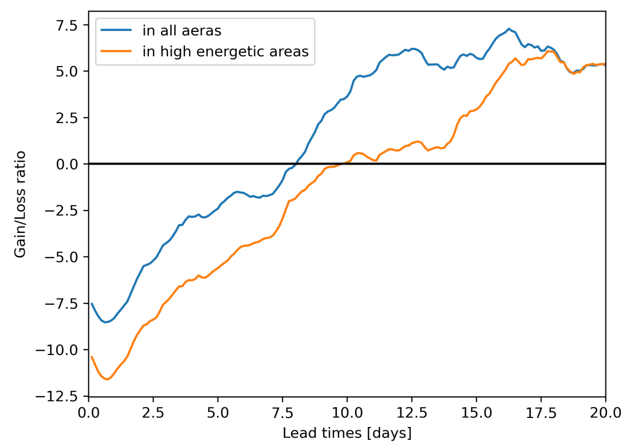

Figure 8. Gain/loss ratio on the predictability of mapped surface geostrophic current for estimating Lagrangian transport, in function of the prediction lead times. Negative values indicate better performances for the BFN-QG method compared to DUACS. In blue, all the drifter data available in the experimental time period are considered. In orange, only the drifters located in the high energetic regions are considered.

systems and the position of one drifter at this date (marked by the red cross). Qualitatively, this figure shows that the currents estimated by the BFN-QG depict finer scale structures (filaments and small vortices) than the ones derived from DUACS.

On the one hand, we perform Eulerian diagnostics by comparing the estimated currents with the velocities measured by the drifters at each location (in space and time) of the drifters. We use the same methodology as for the SLA-mapping per-

https://doi.org/10.5194/egusphere-2023-509
Preprint. Discussion started: 4 April 2023

formances: the mapped velocities (meridional and zonal components) are interpolated on the drifters' locations and the errors with the drifters' velocities are aggregated in 1° longitude x 1° latitude boxes. The RMSE and the gain/loss ratio R (equation 12) are then computed in each box. The geographical distribution of the gain/loss ratio R (figure 7) shows a net improvement of the estimation of both zonal and meridional current. This improvement is more pronounced for the meridional component which is often harder to estimate from altimetry compared to the zonal component due to the nearly meridional orientation of the altimetry tracks. Like the SLA-mapping, more improvements (same as before, it's a relative comparison in %) occur in high variability regions, as shown by the intensification of blue pixels in the inner domain delimited by the green contour on figure 7. Besides, the relative performance of the BFN-QG in low variability regions are better for the V-mapping than for the SLA-mapping. This is probably due to the fact that the low variability dynamics occur at large scales, which have very little impact on geostrophic currents.

On the other hand, we perform Lagrangian diagnostics by comparing simulated drifters' trajectories with the real ones. More precisely, we compute the distances between each drifter's location and the expected locations obtained by advecting past positions by the mapped velocities (with forecast lead times ranging from 0 to 20 days, every 3 hours). The results show that the BFN-QG-derived geostrophic currents improve the prediction of short-term Lagrangian transport compared to the DUACS-derived geostrophic currents. Qualitatively, figure 6 shows that the blue dots, representing Lagrangian predictions with lead time up to 5 days, are much closer to the real location of the drifter for the BFN-QG system than for DUACS. However, the red dots, representing Lagrangian predictions higher than 10 days, are as far as the ones predicted by DUACS. Quantitatively, figure 8 shows that the BFN-QG improves the Lagrangian prediction by more than 7% for 1–3 days lead times compared to DUACS, with an enhanced improvement for drifters located in high variability regions. However, the Gain/Loss ratio becomes positive (which means better performances for DUACS compared to the BFN-QG) for lead times higher than 10 days. Besides, the standard deviation of the Lagrangian errors (not shown) is higher for the BFN-QG than for DUACS, and this is accentuated for long lead times. This is qualitatively visible on figure 6 where the distances between the expected locations and the real location of the drifter increase almost linearly with the lead times for DUACS while they are much more scattered for the BFN-QG (especially for lead times higher than 10 days).

5.2 Validation with SST data

This section compares the positions of fronts and eddies diagnosed from our reconstructions with those diagnosed from high resolution SST observations. To do so, we use the *Fronts Derived from Remote Sensing SST Observations by SEVIRI over Agulhas Region* dataset created within the ESA *World Ocean Circulation* (WOC) project (DOI: 10.12770/6c776c43-425b-4d29-9934-0822696f15d8) as ground-truth. For each point $P_i = \begin{bmatrix} lon_i \\ lat_i \end{bmatrix}$ of the detected frontal structures, we compute the flow crossing the fronts using either BFN-QG or DUACS geostrophic currents:

$$Flow[P_i] = \left| \frac{\boldsymbol{v}[P_i] \cdot \boldsymbol{\delta_i}}{\|\boldsymbol{v}\,[P_i]\| \|\boldsymbol{\delta_i}\|} \right| = |cos\,(\angle(\boldsymbol{v}[P_i], \boldsymbol{\delta_i}))|$$

https://doi.org/10.5194/egusphere-2023-509
Preprint. Discussion started: 4 April 2023

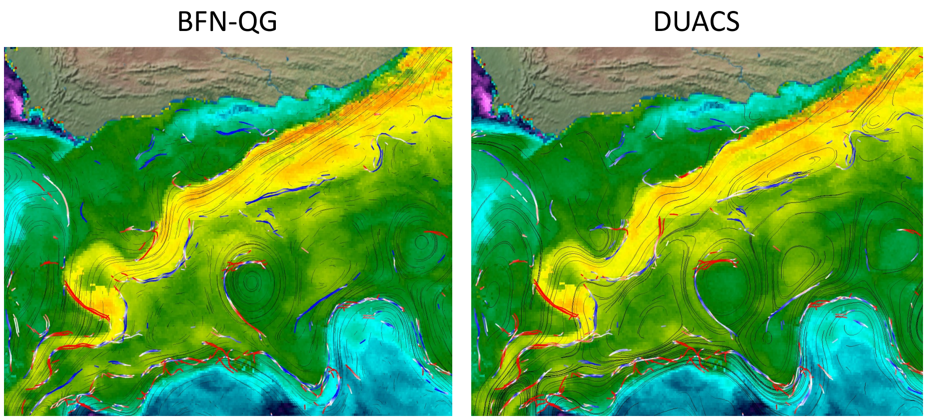

Figure 9. Snapshots showing the geostrophic current streamlines computed from the BFN (left panel) and DUACS (right panel) on top of the SEVIRI SST for which the detected frontal structures are depicted by the colored lines (in blue for small values of the crossing flow, red for high values). These snapshots are taken from the Ocean Virtual Laboratory web portal.

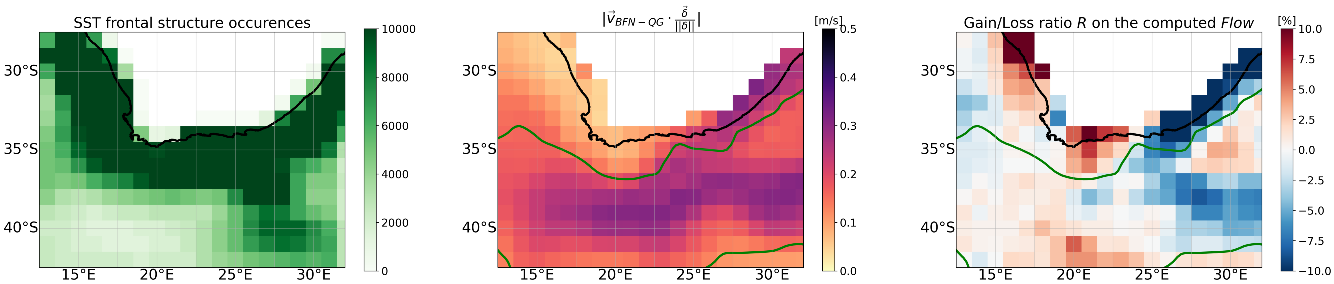

Figure 10. Geographical distribution of: the frontal structure occurrences during the ten years of comparison (left), the averaged BFN-QG currents crossing the SST fronts (middle) and the gain/loss ratio R on the computed $Flow$ (as for figure 4, negative/blue values indicate better performances for the BFN-QG method compared to DUACS). The green contour is the 200 cm^2 SSH variance contour.

where $\boldsymbol{\delta_i} = \begin{bmatrix} lat_{i+1} - lat_{i-1} \\ -(lon_{i+1} - lon_{i-1})cos(lat_i) \end{bmatrix}$ is the normal vector of the front at point P_i. The values of the flow range from 0 to 1. Assuming that the fronts are aligned with the true currents, the smaller the flow, the more consistent the current estimation is to the SST. This hypothesis is not always valid and some preliminary tests must be done to use the fronts for the performance evaluation:

- The advection term must be negligible; this assumption has been checked using the distance travelled by a front within a day.

https://doi.org/10.5194/egusphere-2023-509
Preprint. Discussion started: 4 April 2023

– The SST must be in equilibrium with the currents, only mesoscale sensors are used.

– The SST gradient should be strong enough to be detected automatically

The Agulhas area is a good playground for this kind of analysis, with a strong geostrophic current, strong SST gradients and weak advection of the frontal structures. An illustration of the comparison of fronts and velocity is shown on figure 9. The direction of the streamlines derived from the BFN-QG (left) and DUACS (right) can be compared. One can visually see that the sharp turn of the Agulhas current is better represented in the BFN-QG than in DUACS.

Figure 10 shows statistics of the crossing flow computed from the geostrophic currents derived both from the BFN-QG and DUACS techniques within the 10-years study period. As for the previous diagnostics, the statistics are aggregated in 1° longitude x 1° latitude boxes. The left panel of figure 10 indicates that all pixels of the region are covered by several thousands of SST front occurrences, hence providing reliable statistics. The number of occurrences depends on the probability to detect frontal structures and the cloud cover.

The statistics show mixed performances of the BFN-QG compared to DUACS, with stronger geographical patterns than with the previous diagnostics (see sections 4 and 5). On the one hand, the meanders of the Agulhas current are well captured by the BFN-QG and the improvement in the main current is significant. On the other hand, in some regions, DUACS significantly outperforms the BFN-QG. We note that these regions are mostly characterized by weak crossing currents as shown on the middle panel of figure 10. One example is the Agulhas bank, i.e. the coastal region south of Africa characterized by very shallow waters. In this region, the weak performances of the BFN-QG are probably due to the non representation of the bathymetry in the QG model (whose variations strongly affect the value of the Rossby radius of deformation L_D which modulates the potential vorticity field, through equation 1). This shows that the method needs to be improved to better perform in coastal areas. Finally, figure 10 also depicts weak performances of the BFN-QG (compared to DUACS) in the South-West part of the study domain, in contradiction with the other diagnostics. This can be due to non reliable statistics because of the weaker density of observations and/or too strong advection of the fronts by the currents that limits the validity of the analysis.

6 Discussion and conclusions

In this study, we follow on the analysis presented in Le Guillou et al. (2021a) for assessing the performances of the BFN-QG to map altimetry data. The BFN-QG is a non-common data assimilation technique that can be used to dynamically map altimetry data. This dynamical mapping technique shares similarities with the DOI experimental mapping technique (Ubelmann et al., 2016; Ballarotta et al., 2020). The major advantage of the BFN-QG technique over the DOI technique is the very limited number of parameters to tune and its relatively low numerical cost. Le Guillou et al. (2021a) considered simulated observations for testing the impact of the SWOT mission on the mapping capabilities. Here, the BFN-QG is tested to map real altimetry data in a region covering a part of the highly energetic Agulhas current. The performances are assessed by comparing the mapped products, from BFN-QG and from the operational reference DUACS, with independent datasets. We have carried out diagnostics on mapped SLA (using independent altimetric data) and mapped velocity (using independent drifters and high resolution SST data).

The BFN-QG improves the mapping of short, energetic mesoscale structures both in space and time in comparison with the DUACS system. The BFN-QG is able to reconstruct finer coherent structures that are in phase with observations from independent datasets. The spatial effective resolution is improved by a factor of 20% compared to DUACS. The prediction of Lagrangian transport by the BFN-QG-derived geostrophic currents is improved for for lead times up to 10 days in comparison with the DUACS-derived geostrophic currents

The performances of the BFN-QG are not uniform for all temporal and spatial scales. The method fails to improve the mapping of large mesoscale structures (>300km) in comparison with DUACS. This is corroborated by the poor performances of the BFN-QG-derived currents to estimate the Lagrangian transport for lead times larger than 10 days. Future works should investigate the implementation of a multi-scale nudging whose parameters vary with the space and time scales of the dynamics (Stauffer and Seaman, 1994). This would prevent departure from large scale circulation while maintaining the accuracy of the mapping of small scales.

Another issue with the BFN-QG lies in its poor performances in mapping low energetic dynamics. This disagrees with the previous study of Le Guillou et al. (2021a) which showed similar performances in low and high variability regions. One difference here is that the study region exhibits strong variations in bathymetry, limiting the validity of the Quasi-Geostrophic assumption. Another difference is that the observations contain measurement noise that may become important in low variability region, given the fact that the OI allows better representation of measurement noise (through the observation covariance matrix) than the BFN-QG does (that has only one tunable scalar factor, K). Finally, the observations can contain the signature of non-geostrophic dynamics, such as internal tides, which can be strong in low variability regions (Qiu et al., 2018)). A natural perspective should be to test the method presented in Le Guillou et al. (2021b) to jointly map internal tides and balanced motions from real altimetric observations.

Code and data availability. The along-track SLA (level 3), DUACS gridded SLA and geostrophic currents (level 4) products used in this study are freely available on the CMEMS portal (http://marine.copernicus.eu/). The BFN-QG geostrophic currents and the SST frontal structures are freely available on the WOC portal (https://www.worldoceancirculation.org/). The code of the BFN-QG is available on the Github repository MASSH (https://github.com/leguillf/MASSH).

Author contributions. This work is part of the PhD of FLG supervised by EC and CU. FLG implemented the BFN-QG algorithm and ran the experiments. FLG, LG and MB implemented the validation tools. FLG wrote the paper with contributions from all co-authors.

Competing interests. No competing interests are present.

https://doi.org/10.5194/egusphere-2023-509
Preprint. Discussion started: 4 April 2023

Acknowledgements. This research was partly funded by the European Space Agency through the World Ocean Current project (ESA Contract No. 4000130730/20/I-NB).

References

Amraoui, S., Auroux, D., Blum, J., and Cosme, E.: Back-and-forth nudging for the quasi-geostrophic ocean dynamics with altimetry: Theoretical convergence study and numerical experiments with the future SWOT observations, Discrete and Continuous Dynamical Systems - S, 16, 197–219, https://doi.org/10.3934/dcdss.2022058, 2023.

Auroux, D. and Blum, J.: A nudging-based data assimilation method: the Back and Forth Nudging (BFN) algorithm, Nonlinear Processes in Geophysics, 15, 305–319, https://doi.org/10.5194/npg-15-305-2008, 2008.

Ballarotta, M., Ubelmann, C., Pujol, M.-I., Taburet, G., Fournier, F., Legeais, J.-F., Faugère, Y., Delepoulle, A., Chelton, D., Dibarboure, G., and Picot, N.: On the resolutions of ocean altimetry maps, Ocean Science, 15, 1091–1109, https://doi.org/10.5194/os-15-1091-2019, 2019.

Ballarotta, M., Ubelmann, C., Rogé, M., Fournier, F., Yannice, F., Gerald, D., Morrow, R., and Picot, N.: Dynamic Mapping of Along-Track Ocean Altimetry: Performance from Real Observations, Journal of Atmospheric and Oceanic Technology, 37, 1–27, https://doi.org/10.1175/JTECH-D-20-0030.1, 2020.

Bryden, H., Beal, L., and Duncan, L.: Structure and Transport of the Agulhas Current and Its Temporal Variability, Journal of Oceanography, 61, 479–492, https://doi.org/10.1007/s10872-005-0057-8, 2005.

Ducet, N., Le Traon, P. Y., and Reverdin, G.: Global high-resolution mapping of ocean circulation from TOPEX/Poseidon and ERS-1 and -2, Journal of Geophysical Research: Oceans, 105, 19 477–19 498, https://doi.org/https://doi.org/10.1029/2000JC900063, 2000.

Elipot, S., Lumpkin, R., Perez, R. C., Lilly, J. M., Early, J. J., and Sykulski, A. M.: A global surface drifter data set at hourly resolution, Journal of Geophysical Research: Oceans, 121, 2937–2966, https://doi.org/https://doi.org/10.1002/2016JC011716, 2016.

Ferrari, R. and Wunsch, C.: Ocean Circulation Kinetic Energy: Reservoirs, Sources, and Sinks, Annual Review of Fluid Mechanics, 41, 253–282, https://doi.org/10.1146/annurev.fluid.40.111406.102139, 2009.

Fu, L.-L., Chelton, D. B., Le Traon, P.-Y., and Morrow, R.: Eddy dynamics from satellite altimetry, Oceanography, 23, 14–25, 2010.

Le Goff, C., Boussidi, B., Mironov, A., Guichoux, Y., Zhen, Y., Tandeo, P., Gueguen, S., and Chapron, B.: Monitoring the Greater Agulhas Current With AIS Data Information, Journal of Geophysical Research: Oceans, 126, e2021JC017 228, https://doi.org/https://doi.org/10.1029/2021JC017228, e2021JC017228 2021JC017228, 2021.

Le Guillou, F., Metref, S., Cosme, E., Ubelmann, C., Ballarotta, M., Sommer, J. L., and Verron, J.: Mapping Altimetry in the Forthcoming SWOT Era by Back-and-Forth Nudging a One-Layer Quasigeostrophic Model, Journal of Atmospheric and Oceanic Technology, 38, 697 – 710, https://doi.org/10.1175/JTECH-D-20-0104.1, 2021a.

Le Guillou, F., Lahaye, N., Ubelmann, C., Metref, S., Cosme, E., Ponte, A., Le Sommer, J., Blayo, E., and Vidard, A.: Joint Estimation of Balanced Motions and Internal Tides From Future Wide-Swath Altimetry, Journal of Advances in Modeling Earth Systems, 13, e2021MS002 613:1–17, https://doi.org/10.1029/2021MS002613, 2021b.

Le Traon, P. Y., Nadal, F., and Ducet, N.: An Improved Mapping Method of Multisatellite Altimeter Data, Journal of Atmospheric and Oceanic Technology, 15, 522 – 534, https://doi.org/10.1175/1520-0426(1998)015<0522:AIMMOM>2.0.CO;2, 1998.

Mulet, S., Rio, M.-H., Etienne, H., Artana, C., Cancet, M., Dibarboure, G., Feng, H., Husson, R., Picot, N., Provost, C., and Strub, P. T.: The new CNES-CLS18 global mean dynamic topography, Ocean Science, 17, 789–808, https://doi.org/10.5194/os-17-789-2021, 2021.

Pujol, M.-I., Faugère, Y., Taburet, G., Dupuy, S., Pelloquin, C., Ablain, M., and Picot, N.: DUACS DT2014: the new multi-mission altimeter data set reprocessed over 20 years, Ocean Science, 12, 1067–1090, https://doi.org/10.5194/os-12-1067-2016, 2016.

https://doi.org/10.5194/egusphere-2023-509
Preprint. Discussion started: 4 April 2023

Qiu, B., Chen, S., Klein, P., Wang, J., Torres, H., Fu, L.-L., and Menemenlis, D.: Seasonality in Transition Scale from Balanced to Unbalanced Motions in the World Ocean, Journal of Physical Oceanography, 48, 591 – 605, https://doi.org/10.1175/JPO-D-17-0169.1, 2018.

Stauffer, D. R. and Seaman, N. L.: Multiscale Four-Dimensional Data Assimilation, Journal of Applied Meteorology and Climatology, 33, 416 – 434, https://doi.org/10.1175/1520-0450(1994)033<0416:MFDDA>2.0.CO;2, 1994.

Su, Z., Wang, J., Klein, P., Thompson, A. F., and Menemenlis, D.: Ocean submesoscales as a key component of the global heat budget, 9, 775, https://doi.org/10.1038/s41467-018-02983-w, 2018.

Taburet, G., Sanchez-Roman, A., Ballarotta, M., Pujol, M.-I., Legeais, J.-F., Fournier, F., Faugere, Y., and Dibarboure, G.: DUACS DT2018: 25 years of reprocessed sea level altimetry products, Ocean Science, 15, 1207–1224, https://doi.org/10.5194/os-15-1207-2019, 2019.

Ubelmann, C., Klein, P., and Fu, L.-L.: Dynamic Interpolation of Sea Surface Height and Potential Applications for Future High-Resolution Altimetry Mapping, Journal of Atmospheric and Oceanic Technology, 32, 177 – 184, https://doi.org/10.1175/JTECH-D-14-00152.1, 2015.

Ubelmann, C., Cornuelle, B., and Fu, L.-L.: Dynamic Mapping of Along-Track Ocean Altimetry: Method and Performance from Observing System Simulation Experiments, Journal of Atmospheric and Oceanic Technology, 33, 1691 – 1699, https://doi.org/10.1175/JTECH-D-15-0163.1, 2016.

Welch, P.: The use of fast Fourier transform for the estimation of power spectra: A method based on time averaging over short, modified periodograms, IEEE Transactions on Audio and Electroacoustics, 15, 70–73, https://doi.org/10.1109/TAU.1967.1161901, 1967.